



Revealing sodium storage mechanism in lithium titanium phosphate: Combined experimental and theoretical study

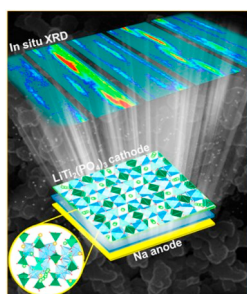
Natalia Voronina, Jae Hyeon Jo, Ji Ung Choi, Aishuak Konarov, Jongsoon Kim **, Seung-Taek Myung *

Department of Nano Technology and Advanced Materials Engineering & Sejong Battery Institute, Sejong University, Seoul, 05006, South Korea

HIGHLIGHTS

- Carbon-coated $\text{LiTi}_2(\text{PO}_4)_3\text{-C}$ shows high conductivity of $\sim 3 \times 10^{-3} \text{ S cm}^{-1}$.
- Two-phase reaction is dominant for $\text{LiTi}_2(\text{PO}_4)_3$ with Li ions to Na ions exchange.
- $\text{LiTi}_2(\text{PO}_4)_3\text{-C}$ exhibits stable cyclability of 94% at 5C over 1000 cycles in Na cells.
- Structural stability is responsible for the extensive cycling at 5C.

GRAPHICAL ABSTRACT



ARTICLE INFO

Keywords:

Sodium-ion batteries
Lithium titanium phosphate
First-principles calculations
Insertion
Ion exchange

ABSTRACT

We investigate a $\text{LiTi}_2(\text{PO}_4)_3$ -carbon composite (LTP-C) with a sodium superionic conductor (NASICON)-type structure as a potential electrode material for sodium storage. *Operando* X-ray diffraction and *ex situ* X-ray absorption spectroscopic analyses reveal that repetitive electrochemical reduction (discharge) and oxidation (charge) between 1.2 and 3.1 V results in a two-phase redox process associated with the $\text{Ti}^{4+}/^{3+}$ redox couple. The rearrangement of the alkali sites during discharge/charge is investigated using first-principles calculations and Rietveld refinement. Using first-principles calculations, we verify the possibility of ion exchange from Li^+ to Na^+ in $\text{LiTi}_2(\text{PO}_4)_3$ in Na cells as well as various theoretical electrochemical properties of $\text{LiNa}_2\text{Ti}_2(\text{PO}_4)_3$ and $\text{Na}_3\text{Ti}_2(\text{PO}_4)_3$. Notably, the sodiated LTP-C exhibits a stable cycle life for over 300 cycles at 0.5C and for over 1000 cycles at 5C with capacity retention of 99% and 94%, respectively.

1. Introduction

$\text{AM}_1\text{M}_2(\text{XO}_4)_3$ fast ionic conductors with three-dimensional (3D) sodium superionic conductor (NASICON)-type structures were first discovered in the mid-1970s by Goodenough et al. [1,2] and have since

attracted considerable interest for application as gas sensors, membranes, fuel cells, and energy storage devices [3–8]. Within this class of materials, the lithium-containing superionic conductor phase $\text{LiTi}_2(\text{PO}_4)_3$ is particularly attractive as a solid-state electrolyte because of its open 3D structure, high ionic conductivity, and thermal and

* Corresponding author.

** Corresponding author.

E-mail addresses: jongsoonkim@sejong.ac.kr (J. Kim), smyung@sejong.ac.kr (S.-T. Myung).

<https://doi.org/10.1016/j.jpowsour.2020.227976>

Received 14 January 2020; Received in revised form 22 February 2020; Accepted 27 February 2020

Available online 5 March 2020

0378-7753/© 2020 Elsevier B.V. All rights reserved.

chemical stability. Its structure includes a 3D framework of phosphate tetrahedra and titanium octahedra that share oxygen vertices. In the crystal structure, six PO₄ tetrahedra surround each TiO₆ octahedron, and four TiO₄ octahedra surround each PO₄ tetrahedron, with the 3D-interconnected channels and interstitial sites occupied by Li ions (commonly referred to as M1 and M2 sites) defined as follows. Namely, the M1 sites (6b, Z = 6) are located in an elongated octahedral oxygen environment at the intersection of three conduction channels, and the M2 sites (18e, Z = 6) are located in an environment of 8–10 oxygen atoms at each bend of the conduction channels. Li ions in LiTi₂(PO₄)₃ selectively occupy only M1 sites. LiTi₂(PO₄)₃ possesses high ionic conductivity with low activation energy for Li⁺ ion diffusion varying from 0.3 to 0.8 eV [9–11]. Aono et al. [12] first showed that the substitution of Ti⁴⁺ in LiTi₂(PO₄)₃ with various trivalent elements leads to structural changes that affect the Li mobility. With Al doping in Li_{1+x}Al_xTi_{2-x}(PO₄)₃ (LATP), the ionic conductivity of the electrolyte increased by almost three orders of magnitude for x = 0.3 [12]. This enhancement was attributed to the increased concentration of Li ions and decreased porosity of the material [12,13].

LiTi₂(PO₄)₃ has been intensively studied not only as a solid electrolyte but also as an electrode material for lithium-ion batteries (LIBs) [14–19,24]. Delmas et al. [14,15] first reported that two Li ions can be reversibly intercalated into the LiTi₂(PO₄)₃ structure in a nonaqueous electrolyte. A flat voltage plateau, attributed to the two-phase reaction between LiTi₂(PO₄)₃ and Li₃Ti₂(PO₄)₃ (Ti^{4+/3+}), was observed at ~2.5 V vs. Li⁺/Li with a theoretical capacity of 138 mAh g⁻¹. Structural refinement of neutron diffraction data revealed that Li ions in Li₃Ti₂(PO₄)₃ fully occupied M2 sites with empty M1 sites in the NASICON structure [15]. LiTi₂(PO₄)₃ suffers from intrinsically poor electronic conductivity, resulting in sluggish kinetic properties, which makes it difficult to attain the theoretical capacity. A combination of nanostructuring and carbon coating is thus usually implemented to increase the electrical conductivity. Kim et al. [16] reported a LiTi₂(PO₄)₃/reduced graphene oxide (rGO) electrode with a capacity of 138 mAh g⁻¹ at 0.1C and superior rate capability up to 100C. In addition, Pan et al. [17] synthesized carbon-coated LiTi₂(PO₄)₃ nanocube composites that exhibited high-rate capability (100 mAh g⁻¹ at 30C) with long-term cyclability. LiTi₂(PO₄)₃ has also been intensively studied as an anode material for rechargeable aqueous LIBs. A LiTi₂(PO₄)₃ anode coupled with a LiMn₂O₄ cathode was tested in an aqueous Li₂SO₄ electrolyte [18], leading to long-term cycling stability at high C-rates with a high areal capacity of 1.2–1.4 mAh cm⁻². Xiang's group also reported excellent electrode performances of NaTi₂(PO₄)₃ and derivatives in protic and aprotic electrolytes [20–23].

Earlier work reported by Aravindan et al. [24] investigated LiTi₂(PO₄)₃ as an electrode material in both LIBs and SIBs. The use of LiTi₂(PO₄)₃ in Na cells resulted in limited capacity in the voltage range of 1.2–3 V (1.59 mol Na⁺ insertion, approximately 110 mAh g⁻¹). Not only LiTi₂(PO₄)₃ (LTP, theoretical capacity: 138 mAh g⁻¹) but also Li_{1+x}Al_xTi_{2-x}(PO₄)₃ (x = 0.3, LATP, theoretical capacity: 117 mAh g⁻¹) are activated by the Ti^{3+/4+} redox pair. Since the amount of Ti in LATP is lower than that of LTP, the resulting theoretical capacity LTP is higher than that of LATP. For this reason, we revisit the LiTi₂(PO₄)₃-carbon composite (LTP-C) as an electrode material for SIBs. The LTP-C electrode delivers a capacity of 136 mAh g⁻¹ and exhibits excellent cycling stability (99% capacity retention after 300 cycles at 0.5C, 69 mA g⁻¹) and high-rate capability (60 mAh g⁻¹ at 30C, 4.14 A g⁻¹) in Na cells. Using first-principles calculations, we predict that Li⁺ ions in LiTi₂(PO₄)₃ can be electrochemically exchanged to Na⁺ ions in Na cells, resulting in slight structural distortion of the rhombohedral structure. Moreover, these theoretical approaches suggest that Na⁺-ion exchanged Na_xTi₂(PO₄)₃ may exhibit outstanding electrochemical performance as a promising electrode material for SIBs. *Operando* X-ray diffraction (XRD) analysis reveals the occurrence of a two-phase reaction, in which Na ions occupy M1 and M2 sites while Li ions migrate to M2 sites. The migrated Li ions are removed from the M2 sites on the subsequent charge, after

which Na ions occupy the M1 sites in the following cycles. These movements of alkali ions are accompanied by the redox reaction of Ti^{4+/3+}, which is stable upon prolonged cycling even at high rates. This outstanding cycling stability is supported by the stable polyanion P–O framework, the structure of which is not altered even after long-term cycling, as evident from transmission electron microscopy (TEM) observation. Herein, we report the details of the structural and electrochemical characteristics of the LTP-C electrode in aprotic Na cells.

2. Experimental

2.1. Synthesis of materials

To obtain LiTi₂(PO₄)₃, Ti(OC₄H₉)₄ (8.78 g, Sigma Aldrich, 97%) in 50 ml of ethanol, mixture of NH₄H₂PO₄ (4.45 g, Samchun, 98%) and LiNO₃ (0.89 g, Sigma Aldrich, 98%) in 20 ml of deionized water were separately prepared. And then the deionized water solution was added to the Ti(OC₄H₉)₄ ethanol solution. The pH value of the obtained solution equaled 6. Then the solution was evaporated at 100 °C, yielding solid resultants. The product was subsequently calcined at 850 °C for 4 h in air (hereafter referred as to be LTP). The obtained LTP powder (5 g) was blended with pitch coke (6 wt %, 28000 MTA, POSCO CHEMICALS, South Korea), and the mixture was heated at 700 °C for 2 h in Ar to prepare the carbon-coated LiTi₂(PO₄)₃ composite (LTP-C).

2.2. Characterization

XRD analysis was performed using a PANalytical X'Pert diffractometer with a Cu Kα source. The samples were scanned in the 2θ range between 10° and 80° using a step size of 0.03°. The FULLPROF program was used to refine the recorded XRD patterns of the LTP and LTP-C powders [25]. The particle surface morphologies were observed using scanning electron microscopy (SEM; SU-8010, Hitachi) and high-resolution TEM (H-800, Hitachi), and elemental mapping was performed using energy-dispersive X-ray spectroscopy (EDX) combined with SEM or TEM. The electrical conductivities of LTP and LTP-C were measured using the standard four-point probe method (CMT-SR1000, AIT). Raman spectroscopy was performed using an inVia Renishaw Raman spectrometer in the region of 500–3000 cm⁻¹. An EA110 elemental analyzer (CE Instruments) was used to determine the amount of carbon in the LTP-C material. Thermogravimetric analysis (TGA) was performed using Trios V3.3 instrument at a heating rate of 10 °C min⁻¹ in an air from 30 to 800 °C. Structural studies during cycling were performed using *operando* XRD (X'Pert, PANalytical) and *ex situ* X-ray absorption near-edge structure (XANES) spectroscopy [26]. XANES measurements were carried out at beamline 8C of the Pohang Accelerator Laboratory (PAL), Pohang, South Korea. The obtained data were analyzed using the Athena software package.

2.3. Electrochemical tests

Electrodes were prepared by mixing 80 wt% of the as-synthesized LTP with 10 wt% of conducting agent (Super P) and 10 wt% polyvinylidene fluoride (PVDF) in *N*-methyl-2-pyrrolidone (NMP). For the LTP-C electrodes, the LTP-C:Super P:PVDF ratio was 84:6:10, i.e., the total carbon content in the electrode composition including the conducting agent was adjusted to 10 wt%. The typical areal mass loading of the active materials is about 5 mg cm⁻². The above mixtures were applied on Al foil with a doctor blade and dried overnight at 100 °C under vacuum. The electrochemical measurements were performed using R2032 coin-type cells consisting of Na metal as the anode, the prepared LTP or LTP-C electrode as the cathode, Whatman GF/C glass fiber as the separator, and 0.5 mol dm⁻³ NaPF₆ solution in a 98:2 vol% mixture of polyethylene carbonate (PC) and fluoroethylene carbonate (FEC) as the electrolyte. All the cells were assembled in an Ar-filled glove box with oxygen and moisture contents below 0.1 ppm. The cycling tests

were conducted in galvanostatic mode between 1.2 and 3.1 V at 25 °C. Galvanostatic intermittent titration technique (GITT) measurements of the electrodes were made at a current density of 0.1C with 30-min discharge or charge and relaxation periods of 1 h.

2.4. Computational details

Density functional theory (DFT) calculations were performed using the Vienna *Ab initio* Simulation Package (VASP) [27]. We used projector-augmented wave (PAW) pseudopotentials [28] with a plane-wave basis set, as implemented in VASP. Perdew–Burke–Ernzerhof (PBE) parametrization of the generalized gradient approximation (GGA) was used for the exchange–correlation functional [29]. The GGA + U method was adopted to address the localization of the *d*-orbital in the Ti ions, with a U value of 4.2 eV, which was set based on previously reported data [30,31]. All the calculations were performed with an energy cutoff of 500 eV until the remaining force in the system converged to less than 0.05 eV/Å per unit cell. Nudged elastic band (NEB) calculations [32] were performed to determine the activation barrier of the Li⁺/Na⁺ ion diffusion in the Na₂LiTi₂(PO₄)₃ and Na₃Ti₂(PO₄)₃ structures. We considered five intermediate states between the first and final images of a single Li⁺/Na⁺ diffusion event. During the NEB calculation, all the structures were allowed to relax within the fixed lattice parameters.

3. Results and discussion

The as-synthesized LTP and LTP-C were crystallized into NASICON-type structures with rhombohedral *R* $\bar{3}c$ space group (Fig. 1a and b). The refined structural parameters determined using the FULLPROF program were consistent with previously reported results [15]. No differences were observed in the parameters of LTP and LTP-C, indicating that the carbon coating did not alter the structure of LTP (Fig. 1a and b and Table S1). The morphology of LTP consisted of spherical particles with primary particle sizes of 100–200 nm (Fig. 1c and S1). TEM–EDX and SEM–EDX mapping revealed homogeneous distributions of Ti, P, and O elements at the nano- and micrometer scales (Fig. 1c and Fig. S1). The high-resolution TEM analysis revealed that the average thickness of the carbon layer was approximately 3 nm (Fig. 1d). The lattice fringe distances deduced from Fig. 1d (lattice image) are 0.6 and 0.42 nm, which are consistent with the (012) and (104) planes of rhombohedral LTP, respectively (Fig. 1d, d-1). The corresponding selected-area electron diffraction (SAED) pattern indexed along the [010] zone axis of LTP

structure confirmed the high crystallinity of the sample and is consistent with the XRD results (Figs. 1d-2). Raman spectra were collected to verify the presence of carbon on the LTP-C surface. The two peaks at 1340 and 1590 cm⁻¹ can be interpreted as D (*sp*³) and G (*sp*²) bands of carbon, respectively (Fig. S2). The appearance of these bands confirms the carbonization of pitch carbon under the applied heat-treatment conditions. The carbon content in LTP-C was determined to be 4.75 and 4.9 wt % using the elemental analyzer and TGA (Fig. S3), respectively. The electrical conductivity of LTP increased from 8 × 10⁻⁶ to 3 × 10⁻³ S cm⁻¹ after the carbon coating was applied (Table S1), which was further demonstrated in ac-impedance data (Fig. S4).

We performed bond-valence sum (BVS) energy map analyses to predict the possible Na⁺ intercalation sites in the rhombohedral LTP structure. The atomic position in the structure was assumed to be affected by the difference in valence of each atom. Fig. 2 shows the three-dimensional diffusion pathways available for Na⁺ insertion into the structure. It was further verified that Na⁺ ions can be intercalated into the vacant sites (M2 sites) with atomic coordinates of (0.333, 0.333, 0.25), denoted as the 18*e* Wyckoff positions, which is different from the existing Li sites (M1 sites) with atomic coordinates of (0, 0, 0), denoted as the 6*b* Wyckoff positions. This finding implies that a total of 3 mol Na ions per formula unit can be theoretically intercalated into the rhombohedral LTP structure.

Based on the structural information for R-LTP, we predicted the theoretical properties of rhombohedral Na_{*x*}LiTi₂(PO₄)₃ (R-NLTP) during Na⁺ intercalation using first-principles calculations. Fig. 3a shows the formation energies of various Na⁺/vacancy configurations of R-NLTP. The redox potential of R-NLTP between each configuration (*V*_{NLTP}) was calculated using the following equation:

$$V_{NLTP} = - \frac{E[\text{Na}_{x_2}\text{LiTi}_2(\text{PO}_4)_3] - E[\text{Na}_{x_1}\text{LiTi}_2(\text{PO}_4)_3] - (x_2 - x_1)E(\text{Na})}{(x_2 - x_1)F} \quad (1)$$

where *E*[Na_{*x*}LiTi₂(PO₄)₃] is the formation energy of the most stable configuration of R-NLTP determined by first-principles calculation, *E*(Na) is the energy of the Na metal, and *F* is the Faraday constant. It was verified that 2 mol Na ions per formula unit can be intercalated in the available voltage range, and the predicted theoretical redox potential of R-NLTP during the intercalation of 2 mol Na⁺ is ~2.06 V (vs. Na⁺/Na), which is consistent with the experimentally measured discharge curve of R-NLTP in a Na cell (Fig. 3b). In addition, we compared the predicted crystal structures of R-Na₂LiTi₂(PO₄)₃ and R-Na₀LiTi₂(PO₄)₃ (Fig. 3c). With Na⁺ intercalation into the structure, large or small displacements

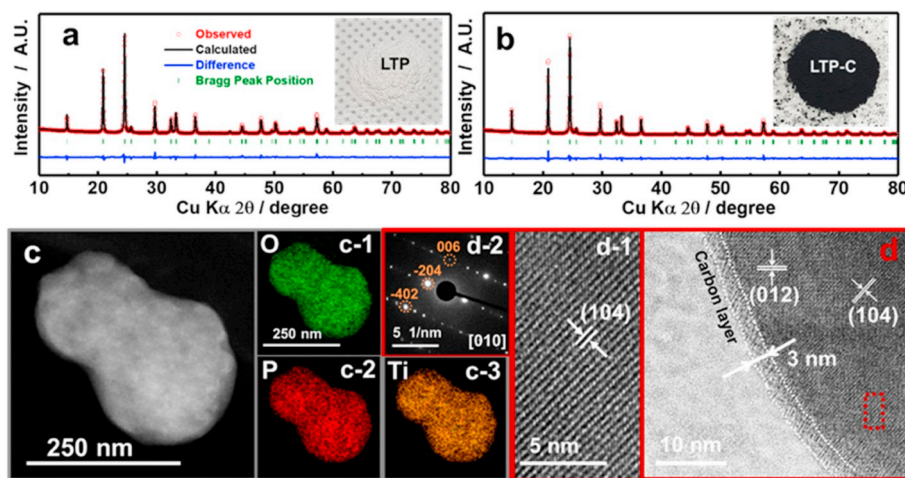


Fig. 1. Rietveld refinement of XRD data for (a) LTP and (b) LTP-C (inset: digital images of corresponding powders) (c) TEM image of LTP and corresponding EDX mappings of (c-1) O, (c-2) P, and (c-3) Ti. (d) Bright-field TEM image of LTP-C, (d-1) HR-TEM image of LTP-C, and (d-2) corresponding SAED pattern along [010] zone axis.

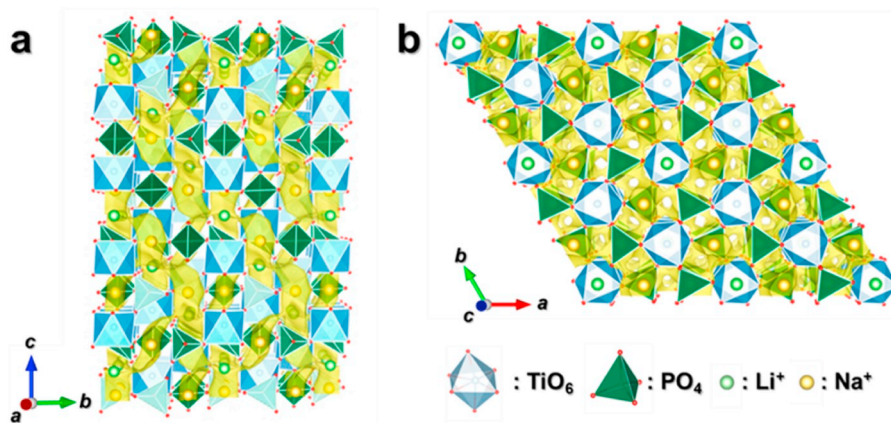


Fig. 2. BVS energy maps of R-LiTi₂(PO₄)₃: (a) bc plane and (b) ab plane.

of all the Li ions from their original positions were observed; in particular, numerous Li ions were shifted from the existing Li site with coordinates of (0, 0, 0) to the vacant site with coordinates of (0.333, 0.333, 0.25), which implies that Na⁺ intercalation into R-NLTP may result in a structural change from the general R-NLTP structure to the slightly distorted rhombohedral Na_xLiTi₂(PO₄)₃ (R'-NLTP) structure. The possibility on Li⁺ migration in R'-NLTP was also verified using the NEB method and first-principles calculation to determine the activation barrier energy for the ionic diffusion. As observed in Fig. 3d, it was predicted that only ~570 meV is required for Li⁺-ion diffusion in the structure, which is sufficiently low for facile Li⁺ migration in R'-NLTP; hence, deintercalation of Li ions and exchange with Na ions, as defined by the insertion of Na ions into Li sites during discharge, are possible in the R'-NLTP structure during charging/discharging in Na cells.

To predict the theoretical properties after the ion exchange from Li⁺ to Na⁺ ions, we performed first-principles calculations on slightly distorted rhombohedral Na_xTi₂(PO₄)₃ (R'-NTP) (1 ≤ x ≤ 3). The formation energies of various configurations of R'-NTP are arranged in Fig. 4a. Because there is no stable intermediate phase between R'-Na₁Ti₂(PO₄)₃ and R'-Na₃Ti₂(PO₄)₃, it was assumed that R'-NTP may undergo a biphasic reaction during Na (de)intercalation. Based on the two end phases of Na₁Ti₂(PO₄)₃ and Na₃Ti₂(PO₄)₃, we calculated the redox potential of R'-NTP (V_{NTP}) using the following equation:

$$V_{NTP} = - \frac{E[\text{Na}_{x_2}\text{Ti}_2(\text{PO}_4)_3] - E[\text{Na}_{x_1}\text{Ti}_2(\text{PO}_4)_3] - (x_2 - x_1)E(\text{Na})}{(x_2 - x_1)F} \quad (2)$$

where $E[\text{Na}_x\text{Ti}_2(\text{PO}_4)_3]$ (1 ≤ x₁ < x₂ ≤ 3) is the formation energy of the most stable configuration of R'-NTP. The predicted potential was verified to be ~1.95 V (vs. Na⁺/Na), which agrees well with the experimental results (Fig. 4b). We verified the appearance of a flat-voltage region of ~1.9 V (vs. Na⁺/Na) in the charge/discharge curve of R'-NTP, which is a typical feature of a biphasic reaction. Fig. 4c shows the thermodynamically most stable crystal structures of R'-Na₁Ti₂(PO₄)₃ and R'-Na₃Ti₂(PO₄)₃. Na⁺ ions in R'-Na₃Ti₂(PO₄)₃ were predicted to be located in the positions neighboring M1 and M2 sites with atomic coordinates of (0, 0, 0) and (0.333, 0.333, 0.25), respectively. After deintercalation of 2 mol Na⁺ from the R'-Na₃Ti₂(PO₄)₃ structure, Na ions may remain near (0, 0, 0), similar to the Li⁺ atomic positions in R-LTP. In addition, we performed NEB calculations to predict the theoretical Na⁺-ion diffusion in the R'-NTP structure. As shown in Fig. 4d, along the Na⁺-Na⁺ pathway with a distance of ~3.15 Å, an activation barrier energy of ~485 meV is required for Na⁺-ion diffusion in the structure, which is lower than that for Li⁺ diffusion (Fig. 4d), implying the sufficiently fast Na⁺-ion hopping.

The electrochemical performances of LTP and LTP-C are compared in Fig. 5. As observed in Fig. 5a, the LTP-C electrode delivered a capacity of 136 mAh g⁻¹ at 0.5C (69 mA g⁻¹), whereas the carbon-free LTP

electrode delivered a low capacity of 50 mAh g⁻¹ at 0.5C. It is evident that the LTP-C electrode was stable over 300 cycles, retaining 99% of its initial capacity. Fig. 5b presents the dQ/dV curves of LTP-C derived from the test results shown in Fig. 5a. The initial insertion of Na ions occurred at approximately 1.9 V, whereas the countering extraction of Na ions was polarized to approximately at 2.4 V, with a gap of 500 mV. Notably, the polarization decreased to 90 mV as cycling progressed; specifically, the average discharge and charge voltages were 2.11 and 2.2 V, respectively, which are identical to those of the Na/NaTi₂(PO₄)₃ cell [31]. The initial differences in the operation voltage are attributed to the structural and thermodynamic limitation of the insertion/extraction of Na ions into/out of the LTP structure, as predicted by first-principles calculations in Figs. 3d and 4d. Fig. 5c and d show the rate performances of the LTP and LTP-C electrodes at currents ranging from 0.5C to 40C. It is apparent that the LTP-C electrode exhibited better rate capability than the carbon-free LTP electrode. The specific capacity of the bare LTP decreased significantly with increasing discharge/charge rates, finally reaching a capacity of only 6 mAh g⁻¹ at 5C. In contrast, the LTP-C electrode exhibited improved performance with increasing current density, maintaining high capacities of 120 mAh g⁻¹ at 5C, 113 mAh g⁻¹ at 10C, 93 mAh g⁻¹ at 20C, and 60 mAh g⁻¹ at 30C. This achievement of high capacities at high rates is responsible for the increase in the electrical conductivity resulting from the presence of electro-conducting carbon layers on the surface of LTP particles. After buffering at 0.5C after the high-rate test at 40C, the initial capacities of both electrodes were recovered, indicating that there was no structural damage to the materials during the high-rate cycling. The LTP-C electrode was cycled at 5C to test its long-term cycling stability; the results confirmed the markedly good capacity retention of 94% after 1000 cycles compared with the capacity of the 25th cycle (Fig. 5e and f). Therefore, the present electrochemical investigation confirms that the crystal structure of LTP-C is substantially stable for long-term cycling even at high rates. Another important conclusion is that the use of a LTP-C electrode in a sodium cell provides a higher reversible capacity than the use of NaTi₂(PO₄)₃ or KTi₂(PO₄)₃ (Table S2). The progressive ion exchange of Li ions into Na ions in the LTP-C electrode that occurred during cycling in the Na cell can be identified as a reliable mechanism for the remarkably stable electrochemical performance.

The crystal structure evolution of the LTP-C electrode in a Na cell was investigated using *operando* XRD analysis during the de-/sodiation processes (Fig. 6). At the initial state of charge, all the reflections of LTP could be indexed to a NASICON structure with the space group of rhombohedral R $\bar{3}c$ except for some peaks from the current collector and beryllium window (Fig. 6a and b). The diffraction peaks at 25.5°, 29.7°, and 33.2° (2 θ) started to immediately shift to lower positions of 24.2°, 29.3°, and 32.4° (2 θ), respectively, as sodiation (reduction) progressed; namely, the phase can be considered sodium-poor Na_xLiTi₂(PO₄)₃. This

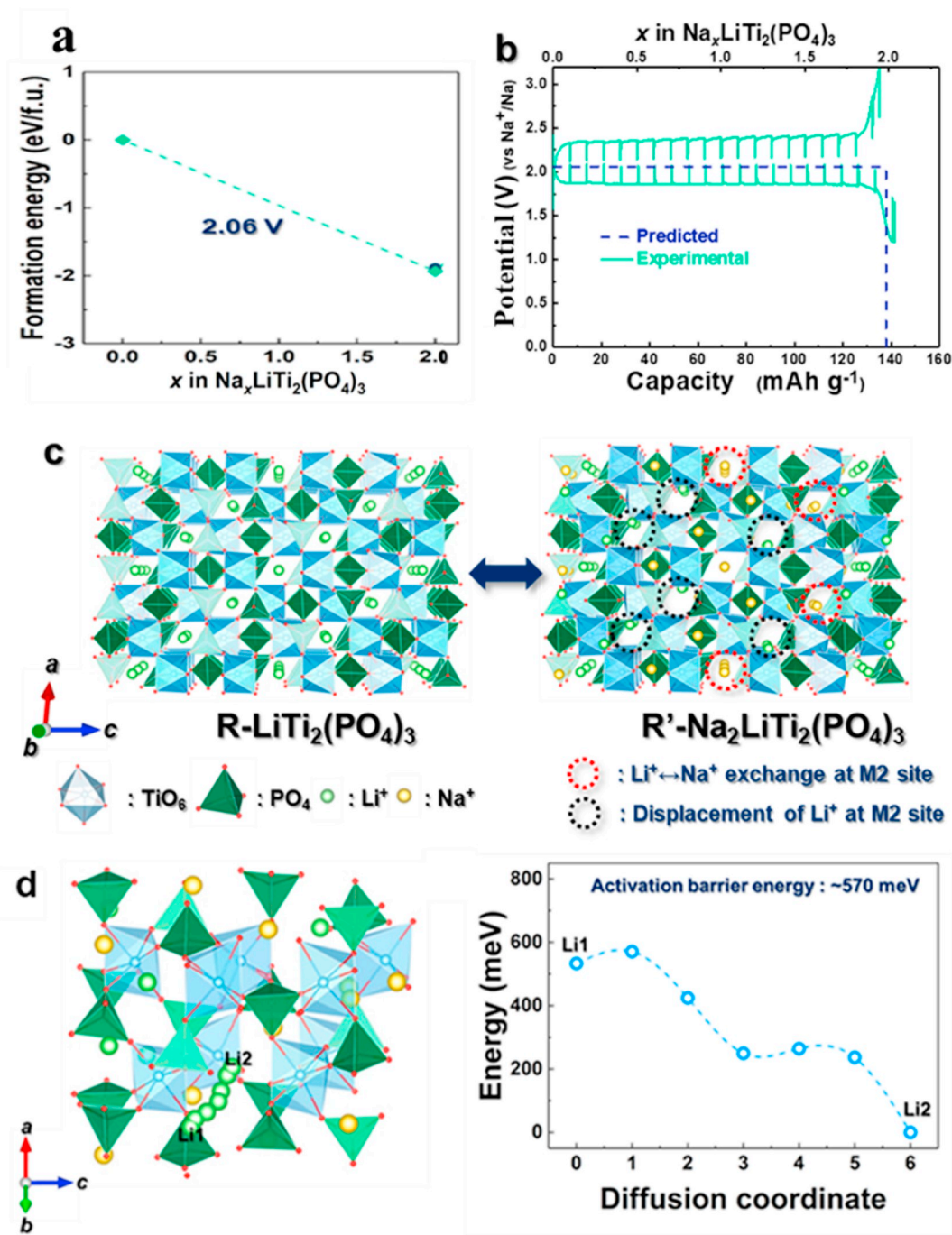


Fig. 3. (a) Formation energies of various configurations of $\text{R-Na}_x\text{LiTi}_2(\text{PO}_4)_3$ ($0 \leq x \leq 3$) with the predicted redox potentials. (b) Comparison between predicted operation potential of $\text{R-Na}_x\text{LiTi}_2(\text{PO}_4)_3$ and experimentally measured discharge/charge GITT curve. (c) Comparison of crystal structures of $\text{R-LiTi}_2(\text{PO}_4)_3$ and $\text{R}'\text{-Na}_2\text{LiTi}_2(\text{PO}_4)_3$. (d) Li–Li diffusion pathways into $\text{R}'\text{-Na}_2\text{LiTi}_2(\text{PO}_4)_3$ and activation barrier energy for Li^+ diffusion in $\text{R}'\text{-Na}_2\text{LiTi}_2(\text{PO}_4)_3$ determined from NEB calculations.

is most likely a sign of the displacement of Li ions along the M1–M2 sites in the 3D diffusion pathway and the preference of Na ions for the M1 site, which affects the transformation into a material with a larger c -axis parameter and unit volume. Further sodiation was involved with the reduction of the newly formed rhombohedral phase observed at 20.7° , 24.2° , 29.3° , 32.4° , and 36.8° (2θ) but produced a new phase at 19.9° , 23.6° , 28.5° , 31.1° , 32.1° , and 35.1° (2θ) with increasing intensities, referred to as sodium-rich $\text{Na}_2\text{LiTi}_2(\text{PO}_4)_3$. At the end of discharge, the rhombohedral $R\bar{3}c$ phase disappeared, indicating the occurrence of a phase transition from the sodium-poor $\text{Na}_x\text{LiTi}_2(\text{PO}_4)_3$ phase to the sodium-rich $\text{Na}_2\text{LiTi}_2(\text{PO}_4)_3$ phase. Rietveld refinement was performed

for the sodium-rich $\text{Na}_2\text{LiTi}_2(\text{PO}_4)_3$ phase assuming the $P\bar{1}$ space group (Fig. 6d). Note that XRD patterns of the rhombohedral phases ($R\bar{3}c$ and triclinic $P\bar{1}$, which is slightly distorted from $R\bar{3}c$ and is referred to as the R' phase in Fig. 3) are almost identical, except for a reflection appearing at 12.2° (2θ) for the $P\bar{1}$ phase that is absent for the $R\bar{3}c$ structure (Figs. S5 and S1). A clearly visible reflection appeared at 12.2° (2θ) for the refined $\text{Na}_2\text{LiTi}_2(\text{PO}_4)_3$ data with lattice parameters $a = 8.8407(4)$ Å, $b = 8.8568(3)$ Å, and $c = 21.6610(3)$ Å, with Li ions located at M2 sites (occupancy 0.333) and Na ions located at both M1 (occupancy 1) and M2 (occupancy 0.333) sites (Fig. 6d, Fig. S3, Table S3). During charging,

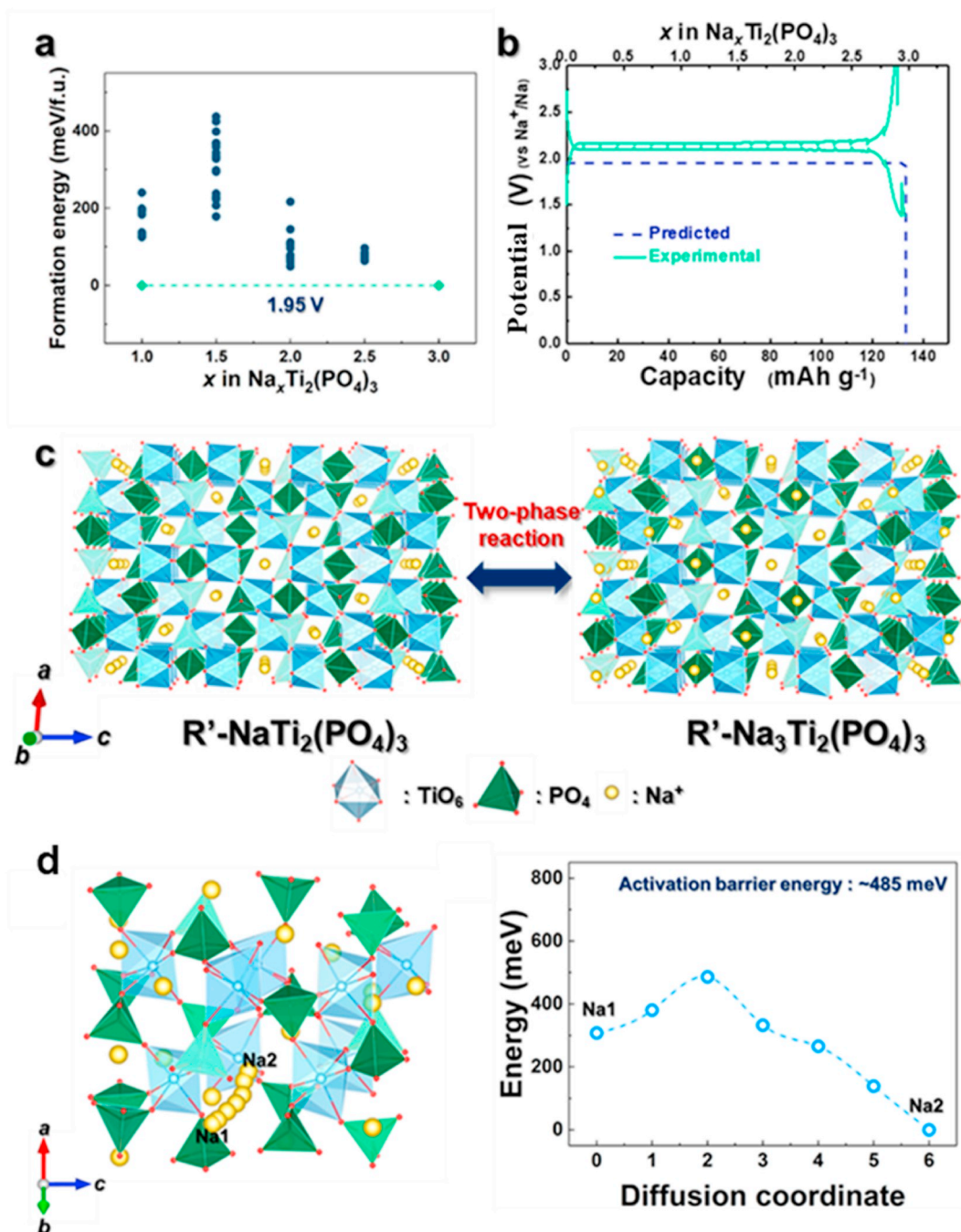


Fig. 4. (a) Formation energies of various configurations of $\text{R}'\text{-Na}_x\text{Ti}_2(\text{PO}_4)_3$ ($1 \leq x \leq 3$) with the predicted redox potentials. (b) Comparison between predicted operation potential of $\text{R}'\text{-Na}_x\text{Ti}_2(\text{PO}_4)_3$ and experimentally measured discharge/charge GITT curve. (c) Comparison of crystal structures of $\text{R}'\text{-NaTi}_2(\text{PO}_4)_3$ and $\text{R}'\text{-Na}_3\text{Ti}_2(\text{PO}_4)_3$. (d) Na–Na diffusion pathways in $\text{R}'\text{-Na}_3\text{Ti}_2(\text{PO}_4)_3$ and (b) activation barrier energy for Na^+ diffusion in $\text{R}'\text{-Na}_3\text{Ti}_2(\text{PO}_4)_3$ determined using NEB calculations.

the intensity of the peaks of the sodium-rich $\text{Na}_2\text{LiTi}_2(\text{PO}_4)_3$ phase started to decrease and the peaks coexisted with the 20.7° , 24.2° , 29.3° , 32.4° , and 36.8° (2θ) peaks of the sodium-poor $\text{Na}_x\text{LiTi}_2(\text{PO}_4)_3$ phase. The sodium-poor $\text{Na}_x\text{LiTi}_2(\text{PO}_4)_3$ phase did not completely transform back into the original $\text{LiTi}_2(\text{PO}_4)_3$ phase at the end of charge, as the characteristic $\text{LiTi}_2(\text{PO}_4)_3$ peaks were not observed at 25.5° , 29.7° , and 33.2° (2θ). This result provides evidence of the reversible two-phase reaction between sodium-poor $\text{Na}_x\text{LiTi}_2(\text{PO}_4)_3$ via electrochemical ion exchange of Li^+ into Na^+ in $\text{LiTi}_2(\text{PO}_4)_3$ and sodium-rich $\text{Na}_2\text{LiTi}_2(\text{PO}_4)_3$ phases, as predicted by the first-principle calculations. The Na ions, and not the Li ions of $\text{Na}_2\text{LiTi}_2(\text{PO}_4)_3$, showed a tendency to be localized at the M1 sites of the rhombohedral NASICON structure after charge,

whereas the Li ions at M1 sites were extracted from $\text{Na}_2\text{LiTi}_2(\text{PO}_4)_3$ to form the electrochemically induced $\text{NaTi}_2(\text{PO}_4)_3$ (Fig. 6e, Table S3). The following sodiation (2nd discharge) again resulted in a two-phase transition from the sodium-poor $\text{NaTi}_2(\text{PO}_4)_3$ ($\text{R}\bar{3}\text{c}$) phase to the sodium-rich $\text{Na}_3\text{Ti}_2(\text{PO}_4)_3$ ($\text{P}\bar{1}$) phase (Fig. 6a and b, Table S3). Rietveld refinement revealed that the lattice parameter and volume of the unit cell after the second discharge were higher than those after the first discharge, which is indicative of the progressive rearrangement of the slightly distorted rhombohedral $\text{R}'\text{-Na}_3\text{Ti}_2(\text{PO}_4)_3$ phase ($\text{P}\bar{1}$) (Fig. 6f, Table S3). The gradual increase/decrease in the discharge/charge voltage to the 20th cycle, identical to those observed in $\text{NaTi}_2(\text{PO}_4)_3$,

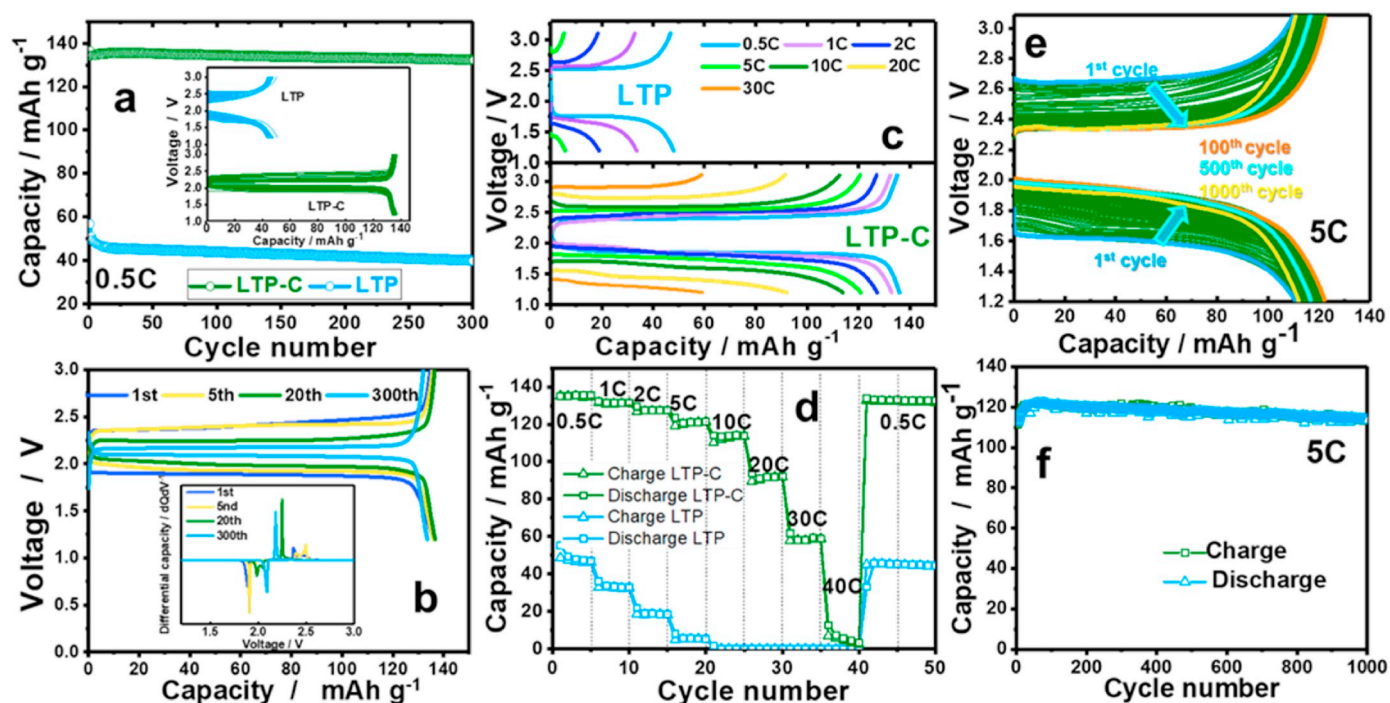


Fig. 5. Electrochemical performance of LTP-C and LTP in Na cells: (a) charge/discharge profiles at 0.5C and corresponding cycling performances; (b) capacity plots and dQ/dV curves of 1st, 5th, 20th, and 300th cycles at 0.5C; (c) charge/discharge profiles and (d) cycling performance at current densities ranging from 0.5C to 40C; (e) charge/discharge profiles at 5C; and (f) corresponding cycling performances.

provides further evidence that the electrochemically induced $\text{Na}_3\text{Ti}_2(\text{PO}_4)_3$ phase behaves progressively, similar to $\text{NaTi}_2(\text{PO}_4)_3$.

Herein, we show that the insertion of 2 mol Na ions per formula unit of $\text{LiTi}_2(\text{PO}_4)_3$ leads to the formation of $\text{Na}_2\text{LiTi}_2(\text{PO}_4)_3$, in which Li ions prefer to be located at M2 sites. In earlier work [15], it was shown that in the $\text{Li}_3\text{Ti}_2(\text{PO}_4)_3$ phase (space group $R\bar{3}$), Li ions are only present within the cavity of the M2 sites. This distribution of Li ions contrasts with that of Na ions in $\text{Na}_3\text{Ti}_2(\text{PO}_4)_3$ ($P\bar{1}$), where both the M1 and M2 cavities are occupied at the same time (M1 occupancy = 1 and M2 occupancy = 0.667) [33]. Our results are thus consistent with previous results and our calculations, with the Li ions preferring to be located at M2 sites and the Na ions preferring to be located at M1 and M2 sites within the $P\bar{1}$ space group in a $\text{Li}_1\text{Na}_2\text{Ti}_2(\text{PO}_4)_3$ compound. These findings are summarized on the right side of Fig. 6b. In addition, these results can potentially be implemented for other NASICON-type materials with mixed ions in the crystal structure.

The changes in the oxidation state of Ti in LTP-C during the discharge/charge process were confirmed by XANES measurements (Fig. 6g). When the cell was discharged to 1.2 V, the Ti K-edge spectrum shifted toward the lower-photon-energy direction compared with that for the fresh LTP-C electrode. This finding indicates that the oxidation state of Ti decreased from tetravalent to trivalent, namely that the spectrum of tetravalent Ti from LTP-C, which is close to the Ti^{4+}O_2 reference, shifted to lower energy and approached that of the Ti^{3+}N reference. After charging to 3.1 V, the spectrum shifted back to higher-photon-energy positions, and the resulting spectrum was identical to that of the fresh state of the LTP-C electrode. It is thus evident that the associated electrochemical reaction is activated by $\text{Ti}^{4+/3+}$ and accompanied by insertion and extraction of Na^+ ions into/from the host materials.

The extensively cycled LTP-C electrode (1000 cycles at 5C) was investigated using XRD and TEM analysis (Fig. 7). The Rietveld refinement data reveal negligible variation in the structure and lattice parameters compared with those after the first cycle (Fig. 7a, Tables S4 and SI). The HRTEM image with lattice fringes with a distance of ~ 0.44 nm

confirm the presence of the (104) lattice plane of $\text{NaTi}_2(\text{PO}_4)_3$ in the cycled LTP-C electrode (Fig. 7, b). The corresponding SAED pattern along the [100] zone axis indicates the high crystallinity of the LTP-C material even after 1000 cycles, confirming maintenance of the original structure after long-term cycling.

4. Conclusion

In summary, we increase the capacity and improve the high-rate stability of $\text{LiTi}_2(\text{PO}_4)_3$ in aprotic Na cells by applying a carbon coating, which increases the electrical conductivity of $\text{LiTi}_2(\text{PO}_4)_3$. The material exhibits a stable cycle life over 300 cycles at 0.5C and over 1000 cycles at 5C with capacity retention of 99% and 94%, respectively. The electrochemical ion exchange of Li ions into Na ions through a two-phase reaction during cycling is predicted by DFT calculations, and the postulated mechanism is experimentally verified using *operando* XRD, Rietveld refinement of the XRD data, and *ex situ* XANES spectroscopy. The excellent structural stability of $\text{LiTi}_2(\text{PO}_4)_3$ in the Na cell during extensive high-rate cycling at 5C is confirmed by *ex situ* XRD and TEM analysis. Our findings will be useful for the development of various hybrid Na/Li electrochemical cells containing Li-based polyanionic cathodes and Na-intercalating anodes or vice versa.

Declaration of competing interest

The authors declare that they have no known competing financial interests or personal relationships that could have appeared to influence the work reported in this paper.

CRediT authorship contribution statement

Natalia Voronina: Conceptualization, Investigation, Writing - original draft, Writing - review & editing. **Jae Hyeon Jo:** Formal analysis. **Ji Ung Choi:** Formal analysis. **Aishuak Konarov:** Formal analysis. **Jongsoo Kim:** Software, Writing - original draft, Writing - review & editing. **Seung-Taek Myung:** Funding acquisition, Conceptualization,

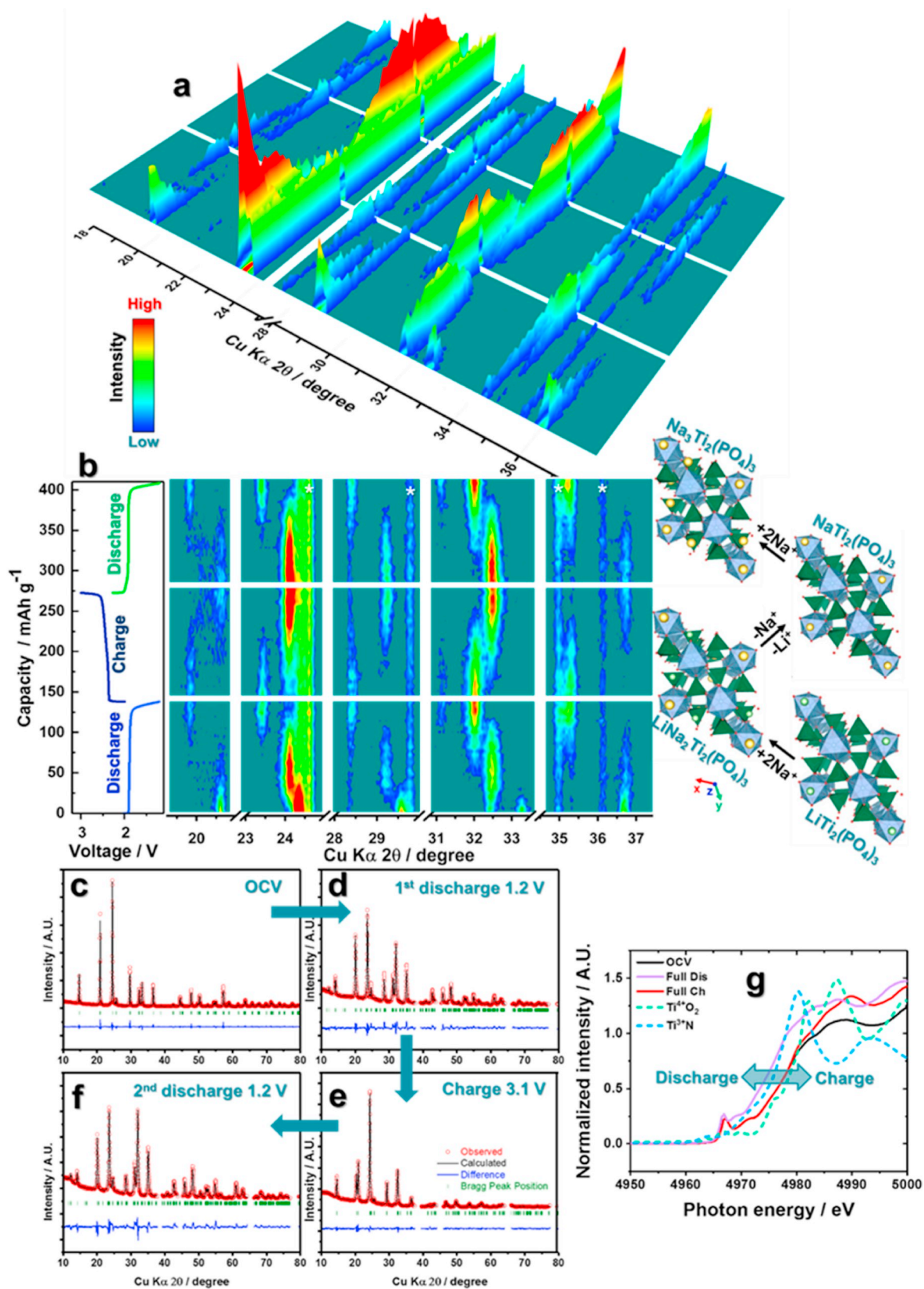


Fig. 6. (a) 3D and (b) 2D images of *operando* XRD data for LTP-C in a Na cell while being discharged/charged/discharged at 0.2C and corresponding *operando* XRD patterns from 18° to 38° (2θ). The Al current collector and Be window are denoted by asterisks. Structural models of the initial LTP and that discharged to 1.2 V, charged to 3.1 V, and second discharged to 1.2 V are shown on the right. *Ex situ* Rietveld refinement of XRD data for LTP-C electrodes (c) at OCV and after being (d) discharged to 1.2 V, (e) charged to 3.1 V, and (f) second discharged to 1.2 V. (g) Ti K-edge XANES spectra of LTP-C electrodes measured at full discharge and full charge.

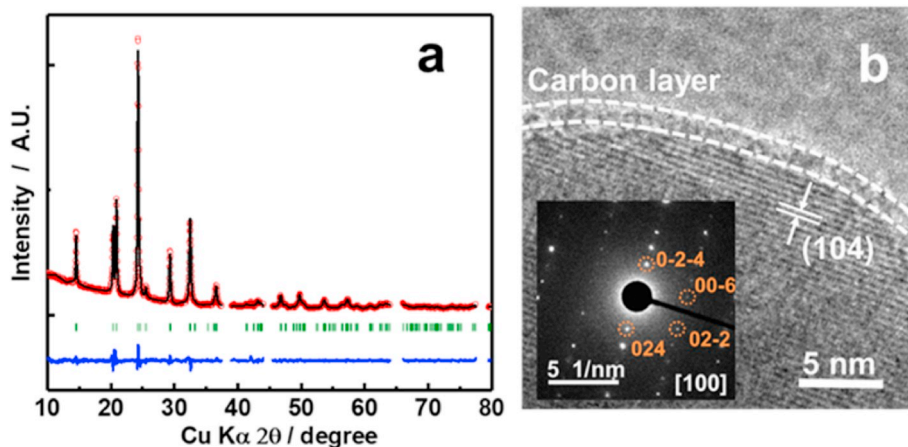


Fig. 7. (a) Ex situ Rietveld refinement of XRD data and (b) TEM image and corresponding SAED pattern along [100] axis of LTP-C electrode after 1000 cycles at 3.1 V.

Writing - original draft, Writing - review & editing.

Acknowledgements

This work was supported by the Basic Science Research Program through the National Research Foundation of Korea (NRF), funded by the Ministry of Education, Science, and Technology of Korea (NRF 2015M3D1A1069713, NRF 2017R1E1A2A01079404, NRF 2017M2A2A6A01070834 and NRF 2017K1A3A1A30084795).

Appendix A. Supplementary data

Supplementary data to this article can be found online at <https://doi.org/10.1016/j.jpowsour.2020.227976>.

References

- [1] H.Y.P. Hong, Crystal structures and crystal chemistry in the system $\text{Na}_{1+x}\text{Zr}_2\text{Si}_x\text{P}_3\text{O}_{12}$, *Mater. Res. Bull.* 11 (1976) 173–182, [https://doi.org/10.1016/0025-5408\(76\)90073-8](https://doi.org/10.1016/0025-5408(76)90073-8).
- [2] J.B. Goodenough, H.Y. Hong, J.A. Kafalas, Fast Na^+ -ion transport in skeleton structures, *Mater. Res. Bull.* 11 (1976) 203–220, [https://doi.org/10.1016/0025-5408\(76\)90077-5](https://doi.org/10.1016/0025-5408(76)90077-5).
- [3] H. Takeda, T. Ueda, K. Kamada, K. Matsuo, T. Hyodo, Y. Shimizu, CO-sensing properties of a NASICON-based gas sensor attached with Pt mixed with Bi_2O_3 as a sensing electrode, *Electrochim. Acta* 155 (2015) 8–15, <https://doi.org/10.1016/j.electacta.2014.12.168>.
- [4] S.A. Dorneanu, I.C. Popescu, P. Fabry, NASICON membrane used as Na^+ -selective potentiometric sensor in steady state and transient hydrodynamic conditions, *Sensor. Actuator. B Chem.* 91 (2003) 67–75, [https://doi.org/10.1016/S0925-4005\(03\)00068-6](https://doi.org/10.1016/S0925-4005(03)00068-6).
- [5] Y. Liu, Q. Sun, Y. Zhao, B. Wang, P. Kaghazchi, K.R. Adair, R. Li, C. Zhang, J. Liu, L. Y. Kuo, Y. Hu, T.K. Sham, L. Zhang, R. Yang, S. Lu, X. Song, X. Sun, Stabilizing the interface of NASICON solid electrolyte against Li metal with atomic layer deposition, *ACS Appl. Mater. Interfaces* 10 (2018) 31240–31248, <https://doi.org/10.1021/acsami.8b06366>.
- [6] J.K. Kim, F. Mueller, H. Kim, D. Bresser, J.S. Park, D.H. Lim, G.T. Kim, S. Passerini, Y. Kim, Rechargeable-hybrid-seawater fuel cell, *NPG Asia Mater.* 6 (2014) e144–e147, <https://doi.org/10.1038/am.2014.106>.
- [7] H. El-Shinawi, A. Regoutz, D.J. Payne, E.J. Cussen, S.A. Corr, NASICON $\text{LiM}_2(\text{PO}_4)_3$ electrolyte ($M = \text{Zr}$) and electrode ($M = \text{Ti}$) materials for all solid-state Li-ion batteries with high total conductivity and low interfacial resistance, *J. Mater. Chem.* 6 (2018) 5296–5303, <https://doi.org/10.1039/c7ta08715b>.
- [8] C. Zhou, S. Bag, V. Thangadurai, Engineering materials for progressive all-solid-state Na batteries, *ACS Energy Lett.* 3 (2018) 2181–2198, <https://doi.org/10.1021/acsenenergylett.8b00948>.
- [9] X. Lu, S. Wang, R. Xiao, S. Shi, H. Li, L. Chen, First-principles insight into the structural fundamental of super ionic conducting in NASICON $\text{MTi}_2(\text{PO}_4)_3$ ($M = \text{Li}, \text{Na}$) materials for rechargeable batteries, *Nano Energy* 41 (2017) 626–633, <https://doi.org/10.1016/j.nanoen.2017.09.044>.
- [10] B. Lang, B. Ziebarth, C. Elsässer, Lithium ion conduction in $\text{LiTi}_2(\text{PO}_4)_3$ and related compounds based on the NASICON structure: a first-principles study, *Chem. Mater.* 27 (2015) 5040–5048, <https://doi.org/10.1021/acs.chemmater.5b01582>.
- [11] G.-Y. Adachi, N. Imanaka, H. Aono, *ADVANCED MATERIALS Fast Li@ Conducting Ceramic Electrolytes*, 1996, pp. 127–135.
- [12] H. Aono, E. Sugimoto, Y. Sadaoka, N. Imanaka, G. ya Adachi, Ionic conductivity and sinterability of lithium titanium phosphate system, *Solid State Ionics* 40–41 (1990) 38–42, [https://doi.org/10.1016/0167-2738\(90\)90282-V](https://doi.org/10.1016/0167-2738(90)90282-V).
- [13] K. Arbi, S. Mandal, J.M. Rojo, J. Sanz, Dependence of ionic conductivity on composition of fast ionic conductors $\text{Li}_{1+x}\text{Ti}_{2-x}\text{Al}_x(\text{PO}_4)_3$, $0 \leq x \leq 0.7$. A parallel NMR and electric impedance study, *Chem. Mater.* 14 (2002) 1091–1097, <https://doi.org/10.1021/cm010528i>.
- [14] C. Delmas, A. Nadiri, J.L. Soubeyroux, The nasicon-type titanium phosphates $\text{ATi}_2(\text{PO}_4)_3$ ($A = \text{Li}, \text{Na}$) as electrode materials, *Solid State Ionics* 28–30 (1988) 419–423, [https://doi.org/10.1016/S0167-2738\(88\)80075-4](https://doi.org/10.1016/S0167-2738(88)80075-4).
- [15] A. Aatiq, M. Ménétrier, L. Croguennec, E. Suard, C. Delmas, On the structure of $\text{Li}_3\text{Ti}_2(\text{PO}_4)_3$, *J. Mater. Chem.* 12 (2002) 2971–2978, <https://doi.org/10.1039/b203652p>.
- [16] H.K. Roh, H.K. Kim, K.C. Roh, K.B. Kim, $\text{LiTi}_2(\text{PO}_4)_3$ /reduced graphene oxide nanocomposite with enhanced electrochemical performance for lithium-ion batteries, *RSC Adv.* 4 (2014) 31672–31677, <https://doi.org/10.1039/c4ra04943h>.
- [17] W. Deng, X. Wang, C. Liu, C. Li, M. Xue, R. Li, F. Pan, Touching the theoretical capacity: synthesizing cubic $\text{LiTi}_2(\text{PO}_4)_3/\text{C}$ nanocomposites for high-performance lithium-ion battery, *Nanoscale* 10 (2018) 6282–6287, <https://doi.org/10.1039/c7nr09684d>.
- [18] J.Y. Luo, Y.Y. Xia, Aqueous lithium-ion battery $\text{LiTi}_2(\text{PO}_4)_3/\text{LiMn}_2\text{O}_4$ with high power and energy densities as well as superior cycling stability, *Adv. Funct. Mater.* 17 (2007) 3877–3884, <https://doi.org/10.1002/adfm.200700638>.
- [19] L. Liu, T. Song, H. Han, H. Park, J. Xiang, Z. Liu, Y. Feng, U. Paik, Electrospun Sn-doped $\text{LiTi}_2(\text{PO}_4)_3/\text{C}$ nanofibers for ultra-fast charging and discharging, *J. Mater. Chem.* 3 (2015) 10395–10402, <https://doi.org/10.1039/c5ta00843c>.
- [20] P. Lei, K. Liu, X. Wan, D. Luo, X. Xiang, Ultrafast Na intercalation chemistry of $\text{Na}_2\text{Ti}_3/2\text{Mn}_{1/2}(\text{PO}_4)_3$ nanodots planted in a carbon matrix as a low cost anode for aqueous sodium-ion batteries, *Chem. Commun.* 55 (2019) 509–512, <https://doi.org/10.1039/c8cc07668e>.
- [21] P. Lei, S. Li, D. Luo, Y. Huang, G. Tian, X. Xiang, Fabricating a carbon-encapsulated $\text{NaTi}_2(\text{PO}_4)_3$ framework as a robust anode material for aqueous sodium-ion batteries, *J. Electroanal. Chem.* 847 (2019), <https://doi.org/10.1016/j.jelechem.2019.05.062>, 113180.
- [22] F. Zhang, W. Li, X. Xiang, M. Sun, Nanocrystal-assembled porous $\text{Na}_3\text{MgTi}(\text{PO}_4)_3$ aggregates as highly stable Anode for aqueous sodium-ion batteries, *Chem. Eur. J.* 23 (2017) 12944–12948, <https://doi.org/10.1002/chem.201703044>.
- [23] W. Zheng, P. Lei, D. Luo, Y. Huang, G. Tian, X. Xiang, Understanding the effect of structural compositions on electrochemical properties of titanium-based polyanionic compounds for superior sodium storage, *Solid State Ionics* 345 (2020), <https://doi.org/10.1016/j.ssi.2019.115194>, 115194.
- [24] V. Aravindan, W.C. Ling, S. Hartung, N. Bucher, S. Madhavi, Carbon-coated $\text{LiTi}_2(\text{PO}_4)_3$: an ideal insertion host for lithium-ion and sodium-ion batteries, *Chem. Asian J.* 9 (2014) 878–882, <https://doi.org/10.1002/asia.201301461>.
- [25] J. Rodríguez-Carvajal, Recent advances in magnetic structure determination by neutron powder diffraction, *Physica B: Phys. Condens. Matter* 192 (1993) 55–69, [https://doi.org/10.1016/0921-4526\(93\)90108-1](https://doi.org/10.1016/0921-4526(93)90108-1).
- [26] B. Ravel, M. Newville, ATHENA, artemis, hephaestus: data analysis for X-ray absorption spectroscopy using IFEFFIT, *J. Synchrotron Radiat.* 12 (2005) 537–541, <https://doi.org/10.1107/S0909049505012719>.
- [27] G. Kresse, J. Furthmüller, Efficiency of ab-initio total energy calculations for metals and semiconductors using a plane-wave basis set, *Comput. Mater. Sci.* 6 (1996) 15–50, [https://doi.org/10.1016/0927-0256\(96\)00008-0](https://doi.org/10.1016/0927-0256(96)00008-0).
- [28] P.E. Blöchl, Projector augmented-wave method, *Phys. Rev. B* 50 (1994) 17953–17979, <https://doi.org/10.1103/PhysRevB.50.17953>.
- [29] J.P. Perdew, K. Burke, M. Ernzerhof, Generalized gradient approximation made simple, *Phys. Rev. Lett.* 77 (1996) 3865–3868, <https://doi.org/10.1103/PhysRevLett.77.3865>.

- [30] B.J. Morgan, D.O. Scanlon, G.W. Watson, Small polarons in Nb- and Ta-doped rutile and anatase TiO₂, *J. Mater. Chem.* 19 (2009) 5175–5178, <https://doi.org/10.1039/b905028k>.
- [31] N. Voronina, J.H. Jo, J.U. Choi, C.H. Jo, J. Kim, S.T. Myung, Nb-Doped titanium phosphate for sodium storage: electrochemical performance and structural insights, *J. Mater. Chem.* 7 (2019) 5748–5759, <https://doi.org/10.1039/c8ta11517f>.
- [32] G. Henkelman, B.P. Uberuaga, H. Jónsson, Climbing image nudged elastic band method for finding saddle points and minimum energy paths, *J. Chem. Phys.* 113 (2000) 9901–9904, <https://doi.org/10.1063/1.1329672>.
- [33] P. Senguttuvan, G. Rousse, M.E. Arroyo Y De Dompablo, H. Vezin, J.M. Tarascon, M.R. Palacín, Low-potential sodium insertion in a nasicon-type structure through the Ti(III)/Ti(II) redox couple, *J. Am. Chem. Soc.* 135 (2013) 3897–3903, <https://doi.org/10.1021/ja311044t>.